JOURNAL OF COMPUTATIONAL PHYSICS **125,** 71–82 (1996)
ARTICLE NO. 0080

Arbitrary Lagrangian–Eulerian Numerical Prediction for Local Scour Caused by Turbulent Flows

SATORU USHIJIMA

Central Research Institute of Electric Power Industry (CRIEPI), 1646 Abiko, Abiko-shi, Chiba-ken, 270-11, Japan

Received January 24, 1995; revised June 16, 1995

A numerical prediction method has been developed for local scour on a sand bed due to turbulent flows on the basis of the arbitrary Lagrangian–Eulerian formulation, in which three-dimensional body-fitted coordinates are properly generated for the sand bed profile unsteadily deformed by the flows. The curvilinear coordinates are generated with reasonable accuracy by means of cubic spline interpolations. The equations for momentum, turbulent quantities, and sand concentration are discretized in a Lagrangian scheme so as to preserve second-order accuracy with respect to time and space. The convection of the variables are evaluated with third-order accuracy, taking account of the velocity of the grid point caused by ALE formulation. On the other hand, the sand bed profiles are predicted with the continuity equation for sand by evaluating the total flux consisting of the bed and suspended loads caused by the tractive and convective forces of the turbulent flows. This prediction method is applied to the results of a three-dimensional local scour experiment. From the comparison with the experimental results, it is verified that the sand bed profiles are satisfactorily predicted and that the predicted results are largely improved compared with those based on the Eulerian coordinate system.

1. INTRODUCTION

Local scour on a sand bed caused by the tractive force of a turbulent flow is considered as one of the practical moving boundary problems. Since in this problem a turbulent flow must be numerically predicted within the three-dimensional computational volume which is unsteadily deformed by the tractive force of the flow itself, it is essential for the numerical prediction to take account of the interaction between a flow field and sand bed deformation.

Some numerical methods were certainly proposed in the past to estimate the local scour due to turbulent flows [1, 2]. However, many of the usual methods employed considerable simplification, such as quasi-three-dimensional models, empirically derived diffusivities, or hydrostatic vertical pressure distributions. Although Olsen and Melaaen [3] recently adopted three-dimensional curvilinear coordinate system, it cannot be applied to unsteady problems. In our previous work [4], on the other hand, while local scour and three-dimensional turbulent flows were unsteadily predicted, there was still some room for improvement owing that the coordinate system is based on Eulerian formulation.

The arbitrary Lagrangian–Eulerian (ALE) method, initially proposed by Hirt [5], has been developed to solve wide-ranging moving boundary problems up to the present, since it is advantageous compared with the Eulerian or Lagrangian coordinate system [6]. In the present numerical prediction method, three-dimensional non-orthogonal curvilinear coordinates are generated so that the coordinate lines are coincident with the deformed sand bed surface on the basis of the ALE formulation. Since cubic spline interpolations are utilized in the present grid generation [7], the numerical representation of the arbitrarily deformed boundary shapes and the evaluation of metric coefficients are more accurate than usual methods [8].

The governing equations for fluid dynamics, including transport equations for turbelence energy, its dissipation rate and suspended loads, are discretized in a Lagrangian scheme [7], so that they can preserve second-order accuracy with respect to time and space. In addition, taking account of the velocity of the grid point, the convection terms in the governing equations are solved with third-order accuracy [9]. Cubic spline interpolations are also made use of to improve the numerical accuracy; the interpolation of physical values in the staggered grid arrangement and the evaluation of derivatives in diffusion terms are all achieved with the spline functions. On the other hand, the sand bed profiles are predicted with the continuity equation for sand by evaluating the total flux consisting of the bed load and suspended load caused by the tractive and convective forces of a turbulent flow.

This prediction method is applied to the results of a three-dimensional local scour experiment. From the comparison with the experimental results, it is verified that the sand bed profiles are satisfactorily predicted by the present method and that the predicted results are largely improved compared with our previous work [4] which was based on the Eulerian coordinate system.

0021-9991/96 $18.00

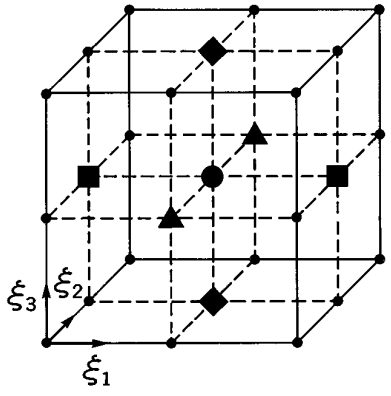

FIG. 1. A unit computational volume in the transformed space (●, scalar value; ■, U_1; ▲, U_2; ♦, U_3).

2. NUMERICAL PROCEDURE

2.1. *Grid Generation*

Let (t, x_1, x_2, x_3) and $(\tau, \xi_1, \xi_2, \xi_3)$ be the time and three-dimensional spatial coordinates in physical and computational (or transformed) spaces, respectively. On the basis of the ALE formulation, the non-orthogonal curvilinear coordinate system (ξ_1, ξ_2, ξ_3) is regenerated for the arbitrarily moving boundaries independently of the fluid motion. The present curvilinear coordinates can be obtained with the following equation which is derived from Poisson equations [8],

$$\left(\frac{\partial^2 x_i}{\partial\xi_p\partial\xi_q}\right)^*\left(\frac{\partial\xi_p}{\partial x_j}\right)^*\left(\frac{\partial\xi_q}{\partial x_j}\right)^* + \frac{\partial^2 x_i}{\partial\xi_r\partial\xi_s}\left(\frac{\partial\xi_r}{\partial x_j}\right)^*\left(\frac{\partial\xi_s}{\partial x_j}\right)^* + P_m\left(\frac{\partial x_i}{\partial\xi_m}\right)^* = 0, \tag{1}$$

where $p \neq q$ and $r = s$ and all subscripts take 1 to 3. The Einstein summation rule is applied to the terms bearing the same subscripts twice in this paper. The control functions P_m are given as exponential forms, which adjust the grid intervals in the physical space [8]. In Eq. (1), the derivatives with asterisks are evaluated not by the usual central difference but from general cubic spline interpolation (GCSI) as proposed by Ushijima [7]. As a result, the metric coefficients are evaluated with higher accuracy than usual method [8].

A unit computational volume in the transformed space consists of 27 grid points, as shown in Fig. 1. All of their locations in the physical space are determined by solving Eq. (1). The scalar variables are placed at the center grid in the unit volume, while each contravariant velocity component is defined at the center grid on the surface normal to its direction. In contrast to such staggered arrangement inside the computational domain, the grid distributions are varied near the boundaries and the physical quantities are defined just on the transformed boundary surfaces so that Dirichlet boundary conditions can be implemented exactly. When a certain physical value at a grid point needs to be evaluated at another grid located in different position, it is interpolated with GCSI in the computational domain rather than simple linear interpolation.

2.2. *Equation of Motion*

The time τ in computational space can be set equal to that of physical space, since there is no need to transform this component in the present problem. Regarding the differentiation of ξ_m with respect to t, in particular, the relationship

$$\frac{\partial\xi_m}{\partial t} = \frac{\partial x_i}{\partial\tau}\frac{C_{im}}{J_E} \equiv u_{0m}\frac{C_{im}}{J_E} \equiv U_{0m} \tag{2}$$

is established, where U_{0m} corresponds to the contravariant component of the grid velocity u_{0m}. In Eq. (2), C_{im} is the cofactor and J_E is the determinant of the Jacobian in the Eulerian coordinates defined by

$$C_{im} = \mathrm{adj}\left[\frac{\partial x_m}{\partial\xi_i}\right] \tag{3a}$$

$$J_E = \det\left[\frac{\partial x_m}{\partial\xi_i}\right]. \tag{3b}$$

Accordingly, in the ALE formulation, the velocity of the grid point must be taken into account in the Lagrangian differentiation in the computational space as

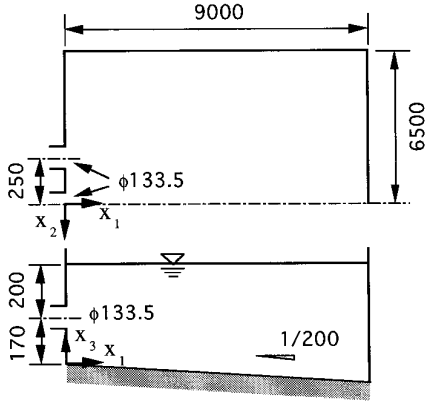

FIG. 2. Schematic view of the experimental flume unit (mm).

$$\frac{D}{Dt} = \frac{\partial}{\partial \tau} + (U_m - U_{0m}) \frac{\partial}{\partial \xi_m}, \tag{4}$$

where U_m is a contravariant component of fluid velocity u_i defined by

$$U_m = u_i \frac{\partial \xi_m}{\partial x_i}. \tag{5}$$

The equations of motion are given as the three-dimensional Reynolds equations which correspond to ensemble-averaged Navier–Stokes equations. When a two-equation turbulence model is employed, the Reynolds equations may be described using the Boussinesq concept with eddy-diffusivity to close the equation system,

$$\begin{aligned} \frac{Du_i}{Dt} = &- \frac{1}{\rho} \frac{\partial p}{\partial \xi_m} \frac{\partial \xi_m}{\partial x_i} + (\nu + \varepsilon_M) \left[\frac{\partial^2 u_i}{\partial \xi_m \partial \xi_n} \frac{\partial \xi_m \partial \xi_n}{\partial x_j \partial x_j} + P_m \frac{\partial u_i}{\partial \xi_m} \right] \\ &\cdot \frac{\partial \varepsilon_M}{\partial \xi_m} \frac{\partial \xi_m}{\partial x_j} \left(\frac{\partial u_i}{\partial \xi_n} \frac{\partial \xi_n}{\partial x_j} + \frac{\partial u_j}{\partial \xi_n} \frac{\partial \xi_n}{\partial x_i} \right) \\ &- \frac{3}{2} \frac{\partial k}{\partial \xi_m} \frac{\partial \xi_m}{\partial x_i} \equiv - PG_i + D_i, \end{aligned} \tag{6}$$

where the Lagrange-differential operator on the left-hand side is given by Eq. (4). On the right-hand side of Eq. (6), PG_i and D_i represent pressure gradient and diffusion terms, respectively. Here u_i, ρ, ν, and ε_M are average velocity in the x_i direction, fluid density, kinematic viscosity, and eddy-diffusivity, respectively. The pressure p corresponds to the deviation from that of the hydrostatic condition. In a $k - \varepsilon$ turbulence model, the turbulent diffusivity

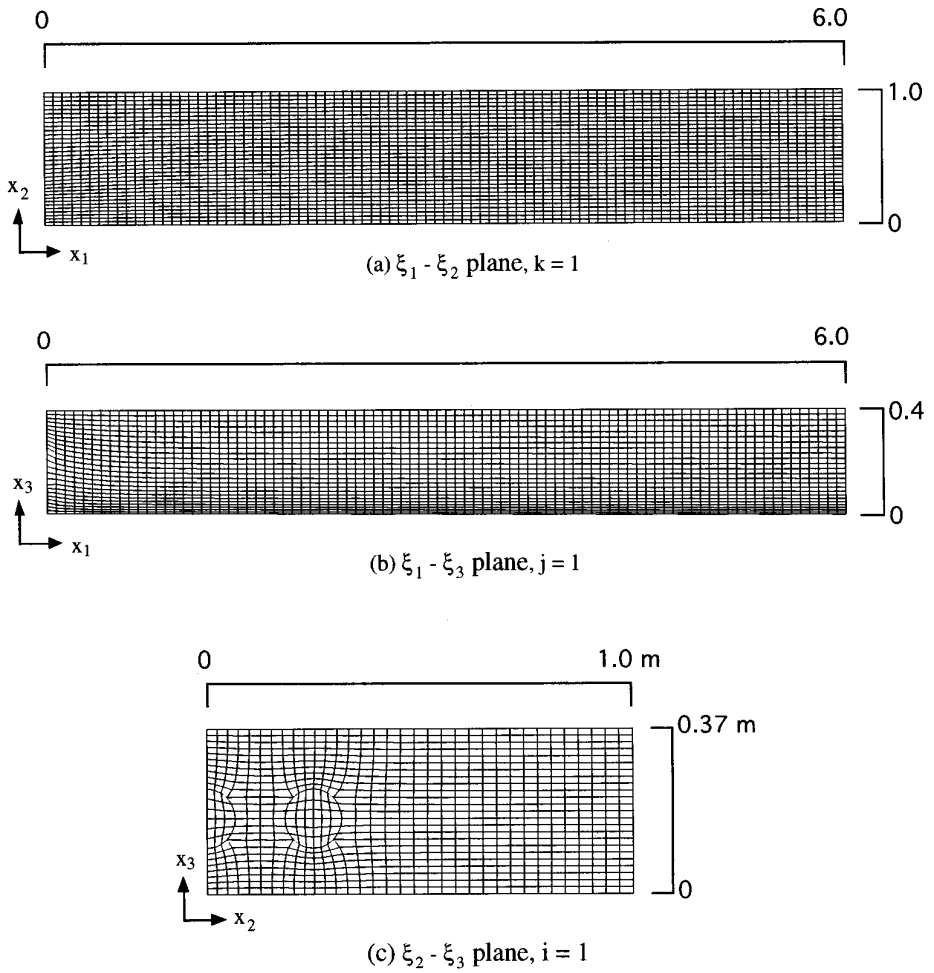

FIG. 3. Generated grid points in the initial stage.

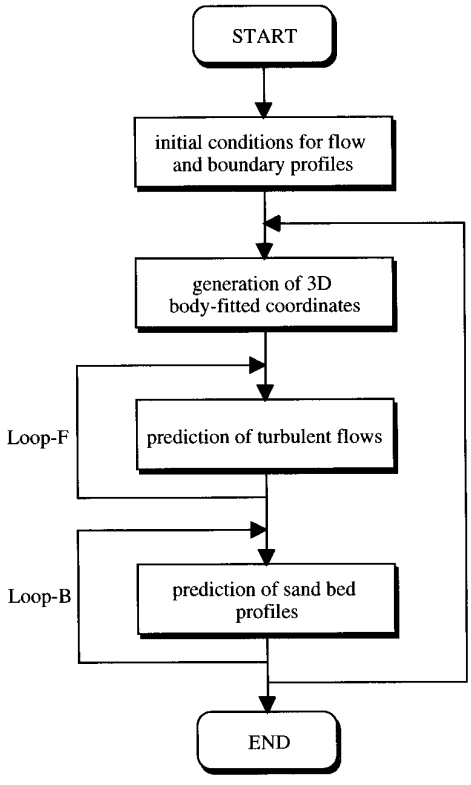

FIG. 4. Outline of the whole numerical procedure.

is given by the following form with turbulence energy k and its dissipation rate ε:

$$\varepsilon_M = C_k \frac{k^2}{\varepsilon}. \tag{7}$$

The momentum equation given by Eq. (6) is discretized in a Lagrangian scheme so as to have second-order accuracy with respect to time and space. The following discretization was applied to a flow field in a curved pipe and it was demonstrated that the secondary flow patterns, as well as the development of the axial velocity distributions, were successfully predicted [7]:

$$u_i^{n+1} = -PG_i^{n+1}\,\Delta t + u_i'^{n} + \left[\frac{3}{2}D_i'^{n} - \frac{1}{2}D_i''^{n-1}\right]\Delta t. \tag{8}$$

The superscripts n stand for the computational time-step number and Δt is the time increment in the calculation. The superscripts "prime" and "double prime" denote the spatial locations at $P'(\xi_1', \xi_2', \xi_3')$ and $P''(\xi_1'', \xi_2'', \xi_3'')$, which correspond to earlier upstream positions specified by

$$\xi_m' = \xi_m - (U_m^n - U_{0m}^n)\,\Delta t \tag{9a}$$

$$\xi_m'' = \xi_m - (U_m^n - U_{0m}^n)\,\Delta t - (U_m'^{n-1} - U_{0m}'^{n-1})\,\Delta t. \tag{9b}$$

The physical values located at P' and P'' are evaluated with a third-order upwind difference [9]. In addition, the derivatives included in the diffusion terms are calculated with GCSI.

The calculation of pressure is substantially the same as done by Ushijima [7].

2.3. *Transport Equation for Turbulent Quantities*

In a computational space, the transport equations for turbulence energy and its dissipation rate may be written as

$$\begin{aligned}\frac{Dk}{Dt} &= \varepsilon_M\left(\frac{\partial u_i}{\partial \xi_n}\frac{\partial \xi_n}{\partial x_j} + \frac{\partial u_j}{\partial \xi_n}\frac{\partial \xi_n}{\partial x_i}\right)\frac{\partial u_i}{\partial \xi_m}\frac{\partial \xi_m}{\partial x_j} \\ &\quad + \left(\nu + \frac{C_k}{C_\nu}\varepsilon_M\right)\left[\frac{\partial^2 k}{\partial \xi_m \partial \xi_n}\frac{\partial \xi_m}{\partial x_j}\frac{\partial \xi_n}{\partial x_j} + P_m\frac{\partial k}{\partial \xi_m}\right] \\ &\quad + \frac{C_k}{C_\nu}\frac{\partial \varepsilon_M}{\partial \xi_m}\frac{\partial \xi_m}{\partial x_j}\frac{\partial k}{\partial \xi_n}\frac{\partial \xi_n}{\partial x_j} - \varepsilon \equiv FK\end{aligned} \tag{10}$$

and

$$\begin{aligned}\frac{D\varepsilon}{Dt} &= C_{\varepsilon 1}\frac{\varepsilon}{k}\varepsilon_M\left(\frac{\partial u_i}{\partial \xi_n}\frac{\partial \xi_n}{\partial x_j} + \frac{\partial u_j}{\partial \xi_n}\frac{\partial \xi_n}{\partial x_i}\right)\frac{\partial u_i}{\partial \xi_m}\frac{\partial \xi_m}{\partial x_j} \\ &\quad + \left(\nu + \frac{C_\varepsilon}{C_\nu}\varepsilon_M\right)\left[\frac{\partial^2 \varepsilon}{\partial \xi_m \partial \xi_n}\frac{\partial \xi_m}{\partial x_j}\frac{\partial \xi_n}{\partial x_j} + P_m\frac{\partial \varepsilon}{\partial \xi_m}\right] \\ &\quad + \frac{C_\varepsilon}{C_\nu}\frac{\partial \varepsilon_M}{\partial \xi_m}\frac{\partial \xi_m}{\partial x_j}\frac{\partial \varepsilon}{\partial \xi_n}\frac{\partial \xi_n}{\partial x_j} - C_{\varepsilon 2}\frac{\varepsilon^2}{k} \equiv FE.\end{aligned} \tag{11}$$

Applying the discretization procedure used to derive Eq. (8), the following results are obtained:

$$k^{n+1} = k'^{n} + \left(\frac{3}{2}FK'^{n} - \frac{1}{2}FK''^{n-1}\right)\Delta t \tag{12}$$

$$\varepsilon^{n+1} = \varepsilon'^{n} + \left(\frac{3}{2}FE'^{n} - \frac{1}{2}FE''^{n-1}\right)\Delta t. \tag{13}$$

In the above equations, all terms included in FK and FE are evaluated with GCSI and the physical values located at P' and P'' are evaluated with a third-order scheme in a manner similar to the momentum equations. The constants, C_k, C_ν, $C_{\varepsilon 1}$, and $C_{\varepsilon 2}$, used in the present turbulence model follow the general values proposed by Rodi [10].

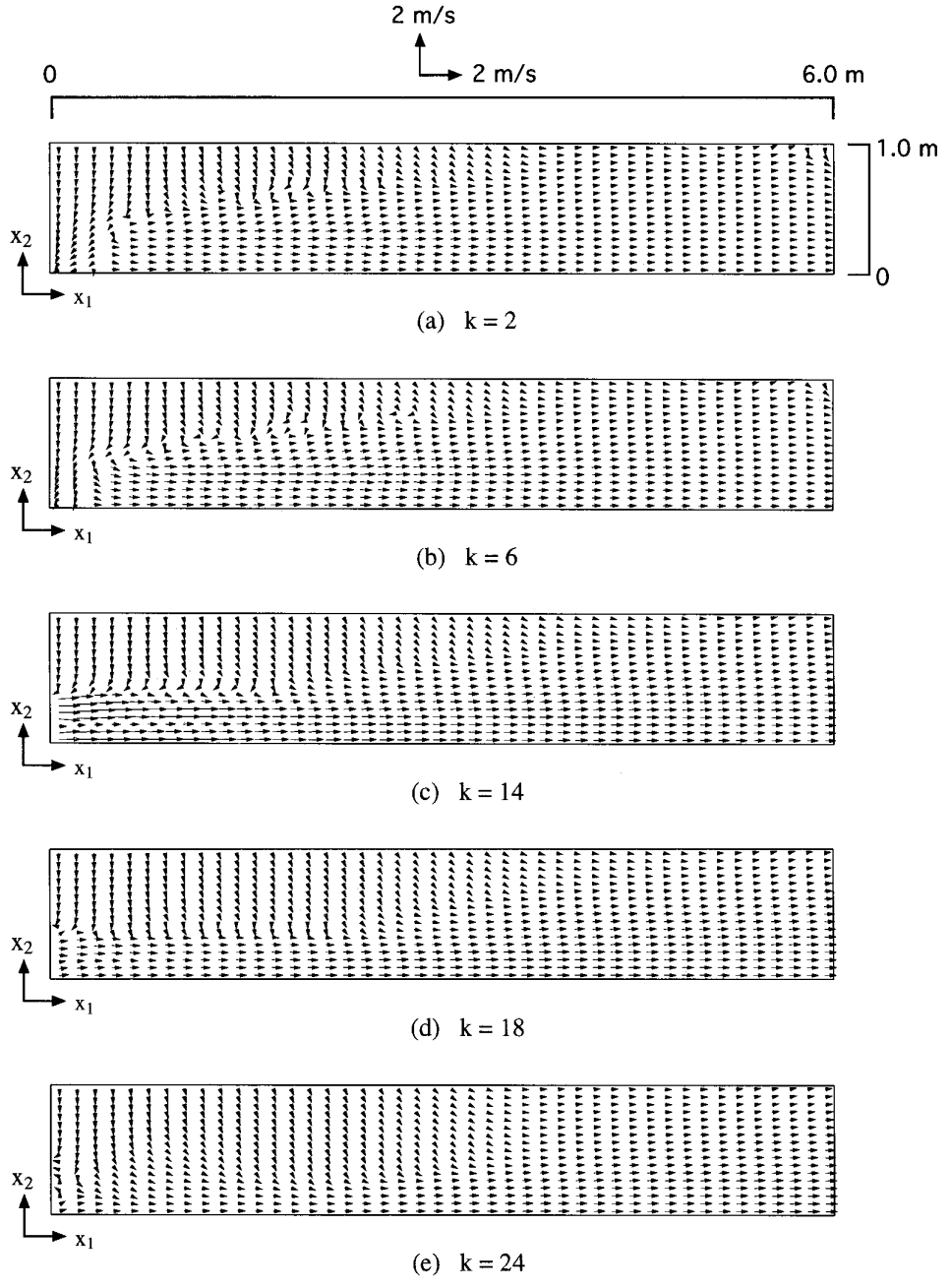

FIG. 5. Predicted velocity vectors ($\xi_1 - \xi_2$ plane, $t = 30$ min).

3. PREDICTION OF SAND BED PROFILE

3.1. *Continuity Equation for Sand*

While a sand bed is unsteadily deformed by the tractive force generated by a turbulent flow, the continuity equation for the transported sand is always satisfied. This continuity equation is utilized to calculate the height of the bed. The transformed continuity equation is written as

$$(1-\gamma)\left(\frac{\partial B}{\partial \tau} - U_{0m}\frac{\partial B}{\partial \xi_m}\right) + \frac{\partial Q_m}{\partial \xi_m} = 0. \tag{14}$$

Here γ, B, and Q_m stand for the porosity of sand, the height of the sand bed, and the total sand flux in ξ_m direction, respectively. The total sand flux is assumed here to be the sum of the bed load Q_{Bm} and suspended load Q_{Sm}:

$$Q_m = Q_{Bm} + Q_{Sm}. \tag{15}$$

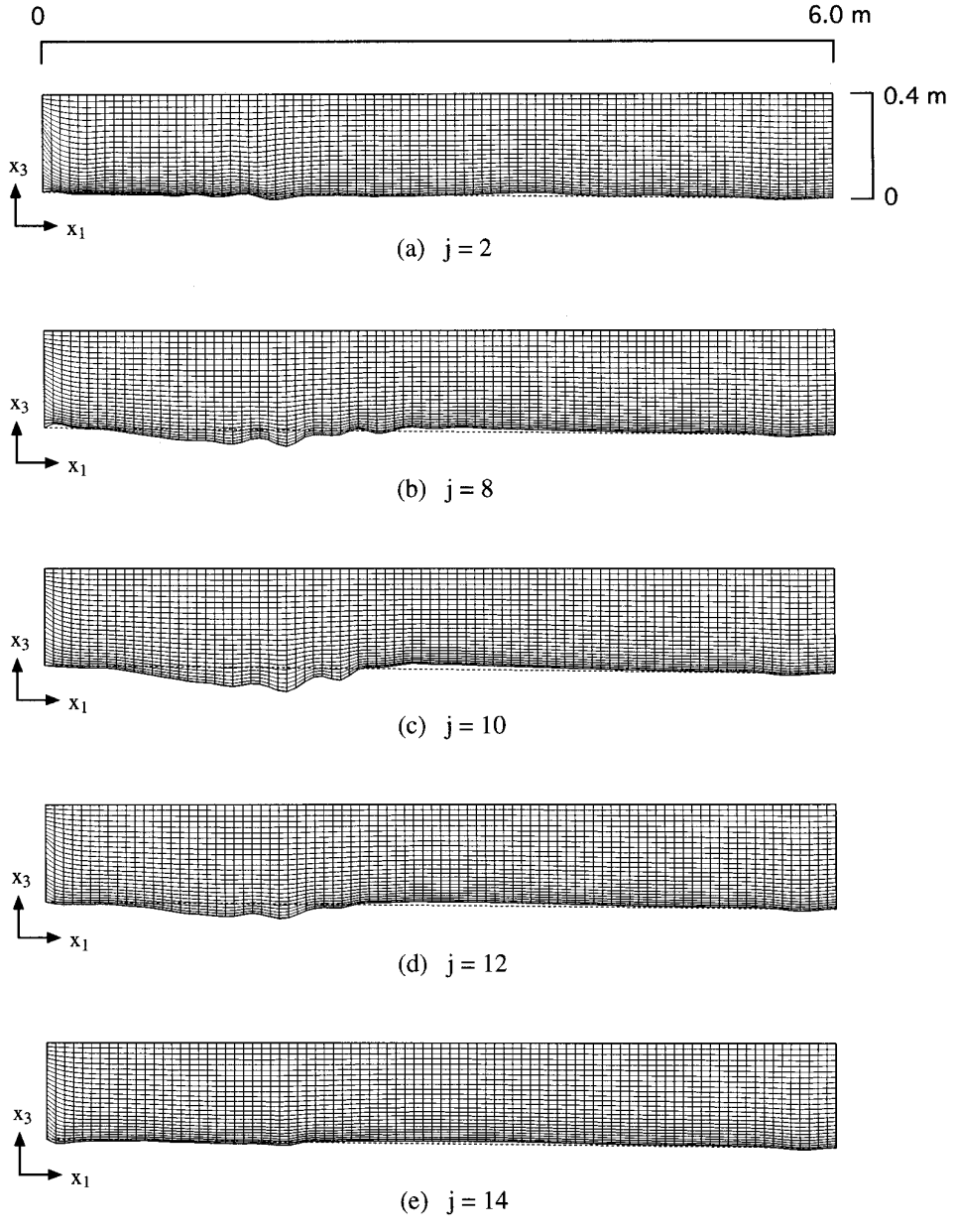

FIG. 6. Distribution of the generated grids ($\xi_1 - \xi_3$ plane, $t = 30$ min).

3.2. *Estimation of Bed Load*

The flux of the bed load Q_{Bm} is calculated from that in the physical space q_{Bi} as

$$Q_{Bm} = q_{Bi} \frac{\partial \xi_m}{\partial x_i}. \tag{16}$$

To evaluate q_{Bi}, some empirical and quasi-theoretical models may be available. Recently Asida *et al.* [11] proposed the relationship

$$\frac{q_{Bi}}{(s\,g\,d)^{1/2}} = 12\tau_{*i}^{3/2}\left(1 - 0.85\frac{\tau_{*c}}{\tau_{*i}}\right)\left(1 - 0.92\frac{u_{*c}}{u_{*i}}\right) \tag{17}$$

with

$$s = \frac{\sigma}{\rho} - 1 \tag{18a}$$

$$\tau_{*i} = \frac{u_{*i}^2}{s\,g\,d} \tag{18b}$$

$$\tau_{*c} = \frac{u_{*c}^2}{s\,g\,d}, \tag{18c}$$

where g, σ, and d are gravity, density, and diameter of sand, respectively. The critical shear stress τ_{*c} and critical friction velocity u_{*c} for sand movement depend on the physical property of sand and fluid viscosity, which can be evaluated from the formulation proposed by Iwagaki [12].

The friction velocity u_{*i} included in Eq. (17) is obtained from the general logarithmic law on the hydraulically rough wall [13], which is given by

$$\frac{u_i}{u_{*i}} = \frac{1}{\kappa}\ln\left(\frac{D}{k_S}\right) + 8.5. \tag{19}$$

Here κ, D, and k_S are the Karman constant, the vertical distance from the sand bed, and the equivalent roughness, respectively.

3.3. *Estimation of Suspended Load*

The transport equation for the concentration of the suspended sediment needs to be solved to estimate Q_{Sm}. The

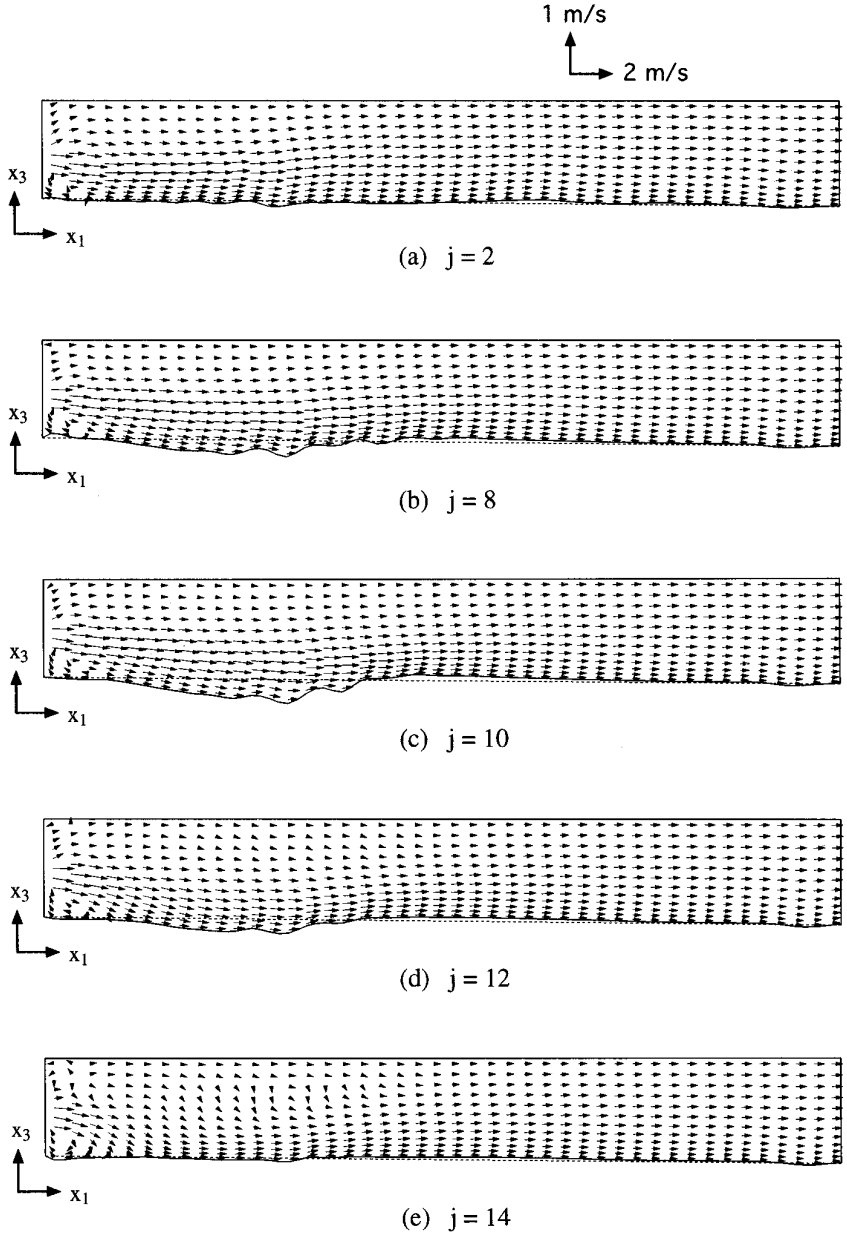

FIG. 7. Predicted velocity vectors ($\xi_1 - \xi_3$ plane, $t = 30$ min).

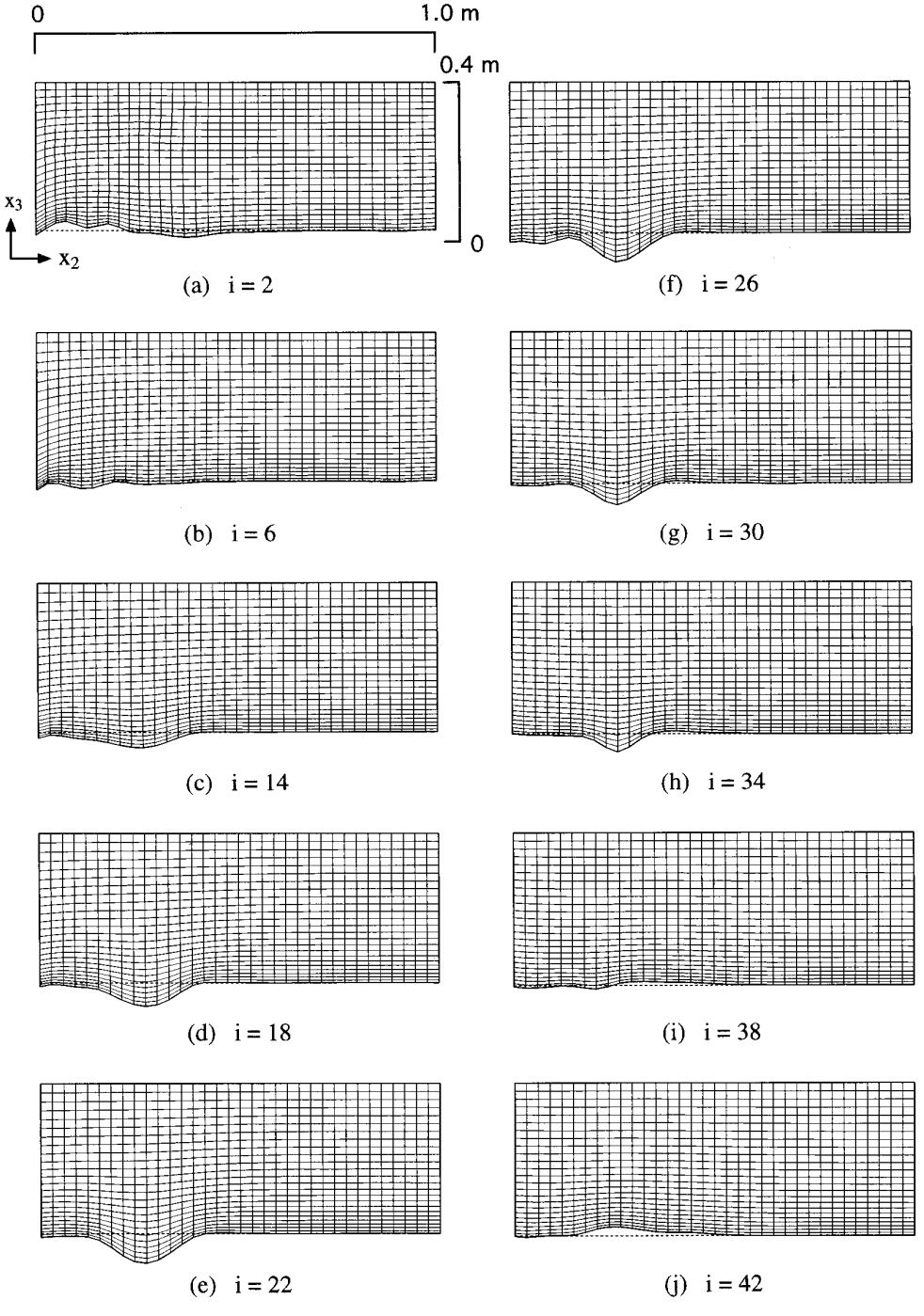

FIG. 8. Distribution of the generated grids ($\xi_2 - \xi_3$ plane, $t = 30$ min).

transport equation can be written in the computational space as

$$\frac{D^*C}{Dt} = (\lambda + \varepsilon_S)\left[\frac{\partial^2 C}{\partial\xi_m\partial\xi_n}\frac{\partial\xi_m\partial\xi_n}{\partial x_j\partial x_j} + P_m\frac{\partial C}{\partial\xi_m}\right] + \frac{\partial\varepsilon_S}{\partial\xi_m}\frac{\partial\xi_m}{\partial x_j}\frac{\partial C}{\partial\xi_n}\frac{\partial\xi_n}{\partial x_j}, \tag{20}$$

where C is the average sand concentration. In Eq. (20), the Boussinesq concept is utilized for the turbulent flux of sand concentration. Here λ and ε_S correspond to the molecular and the turbulent diffusivities, respectively. The Lagrangian differentiation appearing on the left-hand side is defined by

$$\frac{D^*}{Dt} = \frac{\partial}{\partial\tau} + (U_m^* - U_{0m})\frac{\partial}{\partial\xi_m} \tag{21}$$

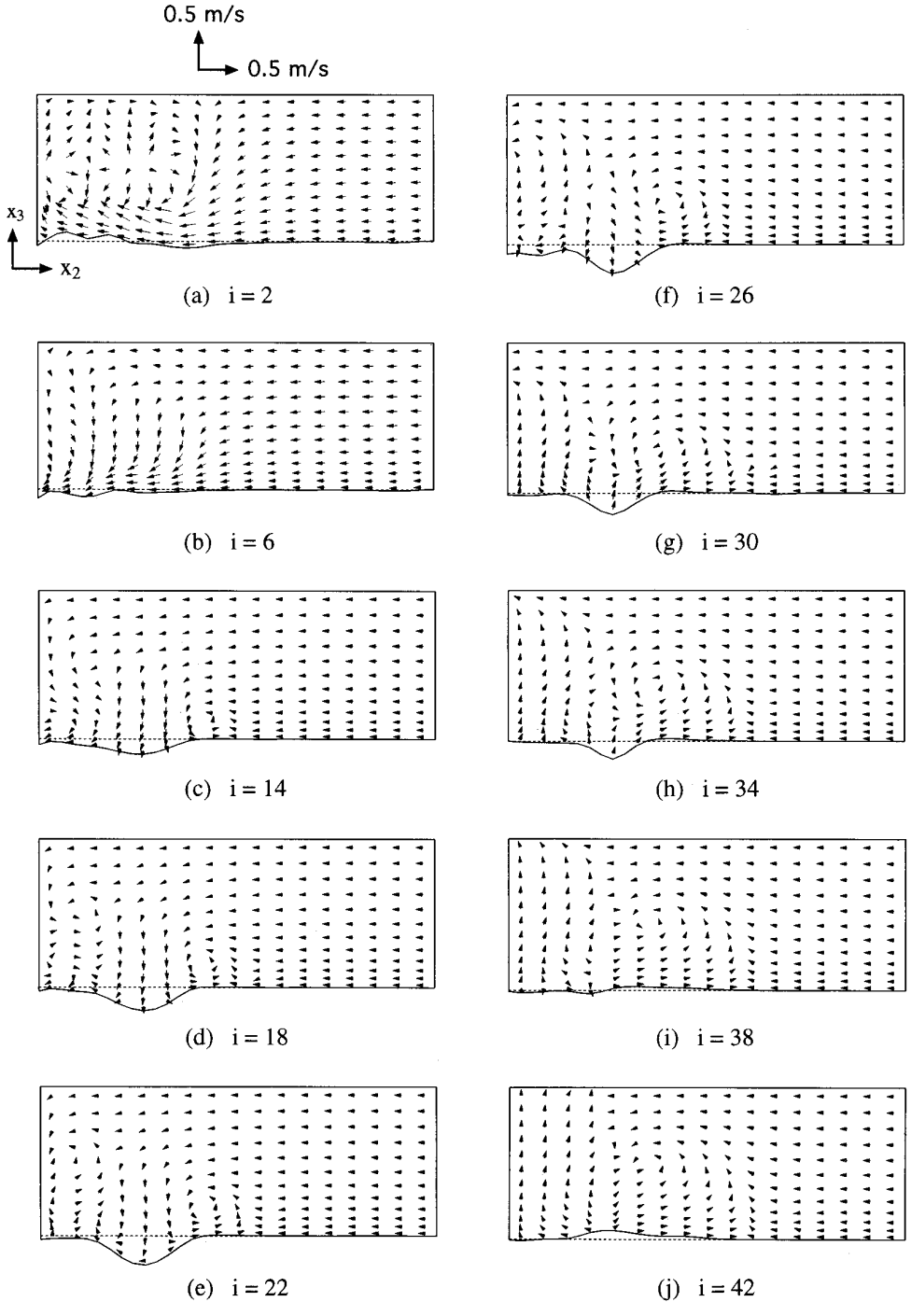

FIG. 9. Predicted velocity vectors ($\xi_2 - \xi_3$ plane, $t = 30$ min).

with

$$U_m^* = (u_j - w_0\delta_{3j})\frac{\partial \xi_m}{\partial x_j}. \tag{22}$$

It is noted that the sedimentation velocity of sand w_0 is taken into account in Eq. (22).

The boundary condition for the sand concentration should be regulated on the bed surface, since the suspended load is generated from the bottom boundary. This boundary condition is given by the model proposed by Lane and Kalinske [14] in the present calculation. The suspended load Q_{Sm} is estimated by integrating in ξ_3 direction the product of C and the corresponding velocity components.

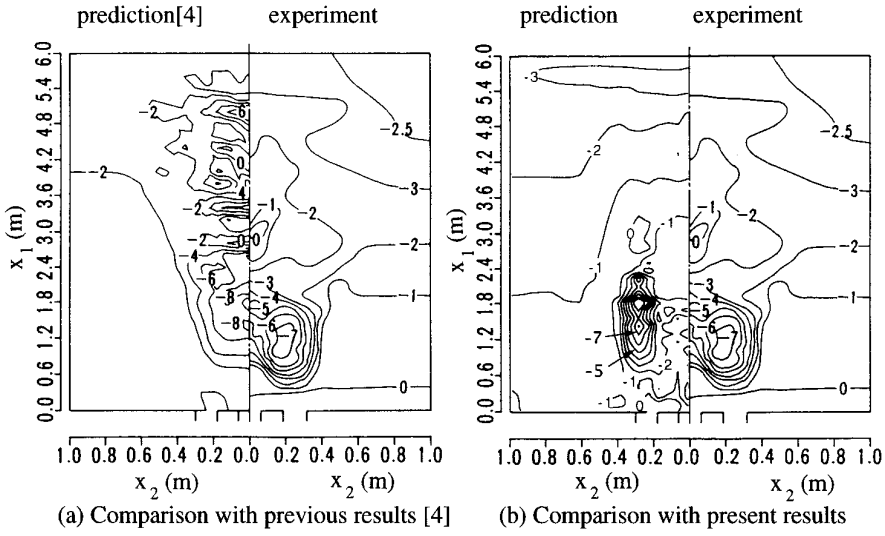

FIG. 10. Contour maps for scoured bed profiles (numbers for lines x_3 (cm); t = 30 min).

4. APPLICATION OF THE PREDICTION METHOD

4.1. *Conditions for Calculation*

The derived numerical prediction method is applied to the three-dimensional local scour experiment which is detailed by Ushijima *et al.* [4]. In this experiment, three jet flows are independently discharged from submerged outlets 133.5 mm in diameter with a flow rate of 4.66×10^{-2} m^3/s in a flat flume 9.0 m in length, 13.0 m in width, and 0.5 m in depth. Nearly uniform sand (density 2.59 g/cm^3 and diameter 0.21 mm) is smoothly spread in the flume with a gradient of approximately 1/200. During the experiment, the sand bed is unsteadily deformed by the tractive force of the discharged jet flows and the bed profile is measured 30 min after the start of the discharge, while the bed deformation has not yet reached equilibrium state at this time.

Figure 2 shows the schematic view of the experimental flume and Cartesian coordinates. The calculation area is set up 6.0 m in x_1 direction and 1.0 m in x_2 direction, assuming the symmetry. Particularly, the shapes of the outlet cross sections and the initial gradient of the bed are exactly treated by means of the curvilinear coordinates. Figure 3 shows the generated curvilinear coordinates at the initial stage.

On the surface, including the center line, symmetrical boundary conditions are applied to the scalar variables and velocity components parallel to it. Free boundary conditions are used on the downstream and side boundaries. On the other hand, wall functions for the hydraulically rough boundaries are adopted on the sand bed and upstream surfaces. The free surface is treated as a rigid boundary with no friction, since the free surface level is nearly constant during the experiment. The total grid number is $\xi_1 \times \xi_2 \times \xi_3 = 89 \times 35 \times 25 = 77{,}875$ and the number of the grids where scalar variables are defined is $45 \times 18 \times 13 = 10{,}530$. This grid number is referred by the indices i, j, and k in ξ_1, ξ_2, and ξ_3 directions, respectively.

The outline of the whole numerical procedure is shown in Fig. 4. After the initial boundary shapes and initial flow conditions are given, three-dimensional body-fitted curvilinear coordinates are first generated. Then the numerical predictions for turbulent flow, including the calculation of Eq. (20), and for sand bed profiles proceed in Loop-F and Loop-B as shown in Fig. 4, respectively. In case that the time scales for the flow field and the sand bed deformation are of the same order, computational time increments for Loop-F and Loop-B (Δt_F and Δt_B, respectively) can be set equal and iteration numbers (k_F and k_B, respectively) may be set unity in both calculations. In this condition, unsteady numerical predictions for fluid and sand bed shapes are simultaneously proceeded and grid generation is performed in every computational step. However, in the present case under consideration, the ratio of the time scales for fluid motion to that for sand bed deformation may be of the order 10^{-5}. Accordingly it can certainly be assumed that the fluid calculation proceeds in Loop-F with a given quasi-static boundary shapes during the deformation is negligible and that the prediction of sand bed profile is performed under a quasi-steady flow patterns in Loop-B as long as the bed deformation does not bring about any effects on the flow field. Taking account of these different time scales, the computational conditions are set at Δt_F = 0.0025 s, Δt_B = 10.0 s, k_F = 2000, and k_B = 45. This condition allows us to get rid of a lot of unnecessary computational time.

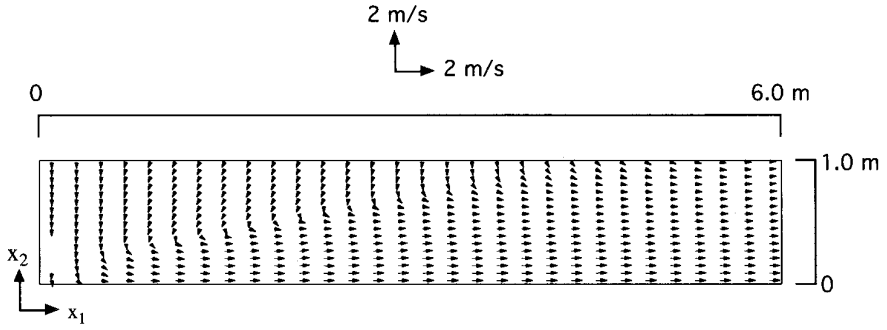

FIG. 11. The velocity vectors predicted by the previous model [4].

4.2. *Comparison with Experimental Results*

The predicted velocity vectors on ξ_1–ξ_2 planes are shown in Fig. 5. The jet flows discharged from different nozzles merge into one primary flow as indicated on Fig. 5c. Near the bottom surface, as shown in Fig. 5a, the effect of the main flow appears at $x_1 \approx 0.5$ m for the first time and the peak velocity arises not on the center line, but at $x_2 \approx 0.25$ m in the downstream region.

Figure 6 shows the generated curvilinear coordinates on ξ_1–ξ_3 planes, in which vertical length scale is magnified by 2.0 times compared with horizontal one. The broken lines in Fig. 6 represent the initial sand bed profile with a gradient of 1/200. As shown in these results, three-dimensional body-fitted coordinates are satisfactorily generated for the deformed sand bed. The deeply scoured area appears at around $\xi_1 = 1.8$ m on $j = 10$ plane as shown in Fig. 6c. Figure 7 shows the predicted velocity vectors on the same ξ_1–ξ_3 planes. The jet flows tend to go toward the bottom surface, probably due to the Coanda effect, which may urge the local scour on the sand bed.

The generated grid distributions on the ξ_2–ξ_3 planes which are vertical to the jet flow axis are shown in Fig. 8. The depression on sand bed is located about 0.25 m apart from the center surface as shown in $i = 18$ to 34 planes in Fig. 8. The secondary flow patterns on the ξ_2–ξ_3 planes are presented in Fig. 9. On the upstream section, as shown in $i = 2$ plane, it can be seen that the entrained secondary flow from the free side boundary forms the slight accumulation of sand near the center region.

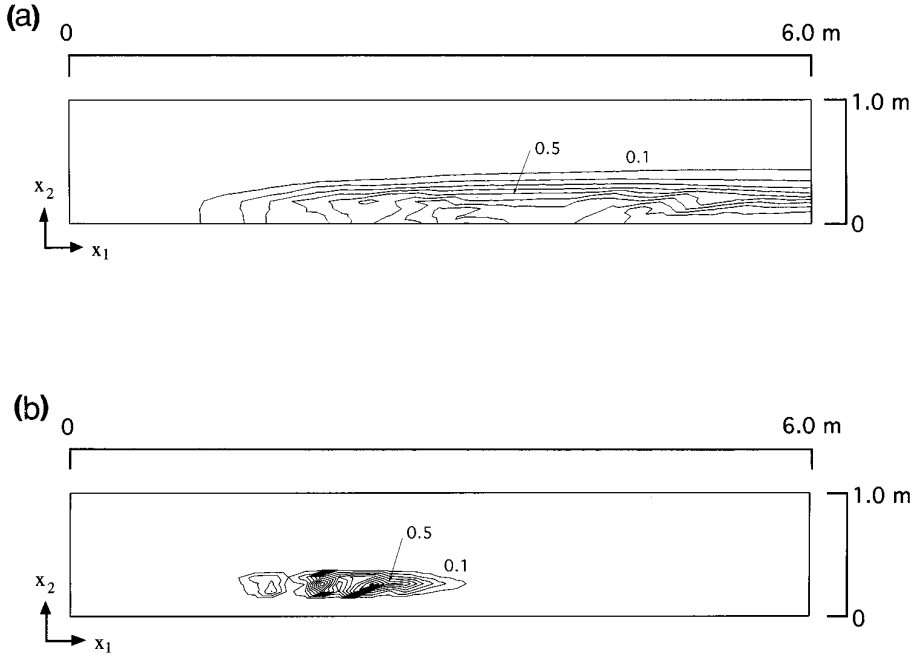

FIG. 12. Nondimensional sand flux (interval of the lines 0.1). (a) Prediction by the previous model [4]; and (b) prediction by the present model.

The predicted sand bed profiles are compared with experimental results in Fig. 10. Figure 10a shows the comparison with the previous numerical results [4], which was obtained with Eulerian grid treatment rather than the present ALE formulation. While the location of the deepest point was near the center line in the previous prediction as shown in Fig. 10a, the location of the sand depression is more precisely predicted in the present numerical result shown in Fig. 10b.

Figure 11 shows the velocity vectors on horizontal surface at $x_3 = 0$, which was obtained in the Eulerian grid formulation. From the comparison with the corresponding result shown in Fig. 5a, it can be seen that the peak velocity appears near the center line in the previous result. Thus the scoured area and the buildup region may occur near the center line in this case as shown in Fig. 10a. On the other hand, in the present result, the maximum velocity arises apart from the center line.

The total sand fluxes, the summation of the bed load and suspended load, are calculated differently between two results as shown in Fig. 12. The total sand fluxes in Fig. 12 are normalized by the maximum values, respectively. In contrast to the previous result, the present numerical model predicts maximum flux apart from the center line, which agrees with the velocity distributions near the bottom surface. It can be concluded that the present sand flux distribution, which mainly results from the accurate prediction for the flow field with curvilinear coordinates, improves the predicted sand bed profiles.

5. CONCLUDING REMARKS

A numerical prediction method for local scour has been developed in the present study on the basis of the arbitrary Lagrangian–Eulerian formulation, in which three-dimensional body-fitted coordinates are properly generated for the sand bed profiles unsteadily deformed by the turbulent flows. The curvilinear coordinates are generated with reasonable accuracy by means of cubic spline interpolations. The equations for momentum, turbulent quantities, and sand concentration are discretized in a Lagrangian scheme so as to preserve second-order accuracy with respect to time and space. The convection of the variables are evaluated with third-order accuracy and the velocity of the grid point caused by the ALE formulation is taken into account. On the other hand, the sand bed profiles are predicted with the continuity equation for sand by evaluating the total flux consisting of the bed and suspended loads caused by the tractive and convective forces of the turbulent flows.

The developed numerical method was applied to a local scour experiment and the predicted sand bed profiles were compared with the measured results. As a result, it is proved that the present numerical method enables us to predict the scoured sand bed profiles satisfactorily.

REFERENCES

1. N. Struiksma, K. W. Olesen, C. Flokstra, and H. J. De Vriend, *J. Hydraul. Res.* **23**(1), 57 (1985).
2. Y. Shimizu, H. Yamaguchi, and T. Itakura, *J. Hydraul. Eng. Am. Soc. Civ. Eng.* **116**(a), 1090 (1990).
3. N. R. B. Olsen and M. C. Melaaen, *J. Hydraul. Eng. Am. Soc. Civ. Eng.* **119**(9) (1993).
4. S. Ushijima, T. Shimizu, A. Sasaki, and Y. Takizawa, *J. Hydraul. Eng. Am. Soc. Civ. Eng.* **118**(8) (1992).
5. C. W. Hirt, A. A. Amsden, and J. L. Cook, *J. Comput. Phys.* **14,** 227 (1974).
6. R. Balasubramaniam, *J. Comput. Phys.* **90,** 396 (1990).
7. S. Ushijima, *Int. J. Numer. Methods Fluids* **19,** 647 (1994).
8. J. F. Thompson, Z. U. A. Warsi, and C. W. Mastin, *Numerical Grid Generation* (Elsevier, New York, 1985).
9. T. Kawamura and K. Kuwahara, AIAA-84-0304, 1984 (unpublished).
10. W. Rodi, ''Turbulence Models and Their Application in Hydraulics,'' in *IAHR Section on Fundamentals of Division II, Experimental and Mathematical Fluid Dynamics, IAHR, Delft, Netherlands, 1980.*
11. K. Ashida, T. Takahashi, and T. Mizuyama, *J. Japan Soc. Erosion Control Eng.* **107** (1978).
12. Y. Iwagaki and Y. Tsuchiya, *Trans. Japan Soc. Civ. Eng.* **41,** 1 (1956).
13. J. Nikuradse, *VDI-Forsch.* **361** (1933).
14. E. W. Lane and A. A. Kalinske, *Trans. Am. Geophys. Union* **22,** 603 (1941).